We are IntechOpen,
the world's leading publisher of Open Access books
Built by scientists, for scientists

6,900
Open access books available

185,000
International authors and editors

200M
Downloads

154
Countries delivered to

Our authors are among the

TOP 1%
most cited scientists

12.2%
Contributors from top 500 universities

BOOK CITATION INDEX INDEXED
CLARIVATE ANALYTICS

WEB OF SCIENCE™

Selection of our books indexed in the Book Citation Index
in Web of Science™ Core Collection (BKCI)

Interested in publishing with us?
Contact book.department@intechopen.com

Intense Aerial Ultrasonic Source and Removal of Unnecessary Gas by the Source

Hikaru Miura
Nihon university
Japan

1. Introduction

Ultrasonic energy is widely used with liquids and solids, for example, for cleaning substances in liquids, atomization of liquids (Miura, 2007b), (Ueha et al., 1985), sedimentation of dispersed fine particles (Miura, 2004), deflection of water (Ito, 2005) , removal of liquid in a pore (Ito & Takamura, 2010), and cutting (Asami & Miura, 2010, 2011) and welding solids (Miura, 2003, 2008). In addition, it is also used with gases, for example, to enhance the removal of unnecessary gases (Miura, 2007a), (Kobayashi et al., 1997), the aggregation and removal of airborne substances such as smoke, antifoaming, drying of wet substances containing moisture, thawing of frozen materials, and the decomposition of methane hydrates (Miura et al., 2006). However, extremely intense sound waves (with a sound pressure of at least 160 dB) are required to perform the above processes in air. Therefore, intense aerial ultrasonic sources are required so that ultrasonic waves can be used in air. Unfortunately, such ultrasonic sources have seldom been developed because it is difficult to generate intense ultrasonic waves in air.

In this chapter, I describe the structure of an ultrasonic source with a flexurally vibrating plate that can radiate extremely intense ultrasonic waves in air as well as the vibration distribution and directivity of the radiated ultrasonic waves. Next, I examine the effect of using the above-mentioned intense aerial ultrasonic source on the enhancement of the removal rate of an unnecessary gas in air. In general, some gas components in air may have adverse effects on humans and the environment, causing environmental problems. Currently, gas absorption, in which a gas is dissolved in a liquid for transport, is widely adopted as a means of collecting gas components in a mixed gas and removing unnecessary gas components. General absorption systems are roughly classified into gas-dispersion-type systems, in which a gas is dispersed in a liquid in the form of microbubbles, and liquid-dispersion-type systems, in which a liquid is sprayed into containers filled with the gas. Both systems allow the gas and liquid to come into contact without applying an external force.

I attempted to enhance the effect of gas absorption by applying ultrasonic waves to such systems. In this chapter, I describe a method of allowing liquid mist obtained using aerial ultrasonic waves to absorb a gas.

2. Intense aerial ultrasonic source

2.1 Outline

Ultrasonic sources using a thin metal plate that vibrates flexurally can be used to radiate extremely intense ultrasonic waves in air. Such ultrasonic sources consist of a longitudinal vibration transducer, a horn for increasing the amplitude, and a flexurally vibrating plate attached at the end of the horn. The length and width of the flexurally vibrating plate are sufficiently greater than the wavelength of flexural vibration, and the plate shape may be square, rectangular, or circular. Flexural vibration is usually generated by vibrating the center of the plate (Miura & Honda, 2002). Such ultrasonic sources can efficiently radiate sound waves in air and achieve a high electroacoustic conversion efficiency by generating an appropriate mode of vibration, i.e., a vibration mode in which the vibration nodes are distributed in a lattice pattern for square plates, a striped pattern for rectangular plates, and a concentric circular pattern for circular plates (Onishi & Miura, 2005), (Miura & Ishikawa, 2009).

In this section, I describe a method for designing a square plate that vibrates flexurally in the lattice mode and can be used as an ultrasonic source, and I discuss the vibration mode of the fabricated plate (Miura, 1994). Next, the measured distributions of vibration displacement and sound pressure near the plate surface are described. Moreover, the directivity of the sound waves radiated from the vibrating plate into remote acoustic fields is theoretically and experimentally examined.

2.2 Intense aerial ultrasonic source

Figure 1 shows a schematic diagram of an ultrasonic source that can radiate intense ultrasonic waves in air. As shown in the figure, the ultrasonic source consists of a longitudinal vibration transducer, a horn for increasing the amplitude, a rod for tuning the resonance of the longitudinal vibration, and a flexurally vibrating plate attached at the end of the horn.
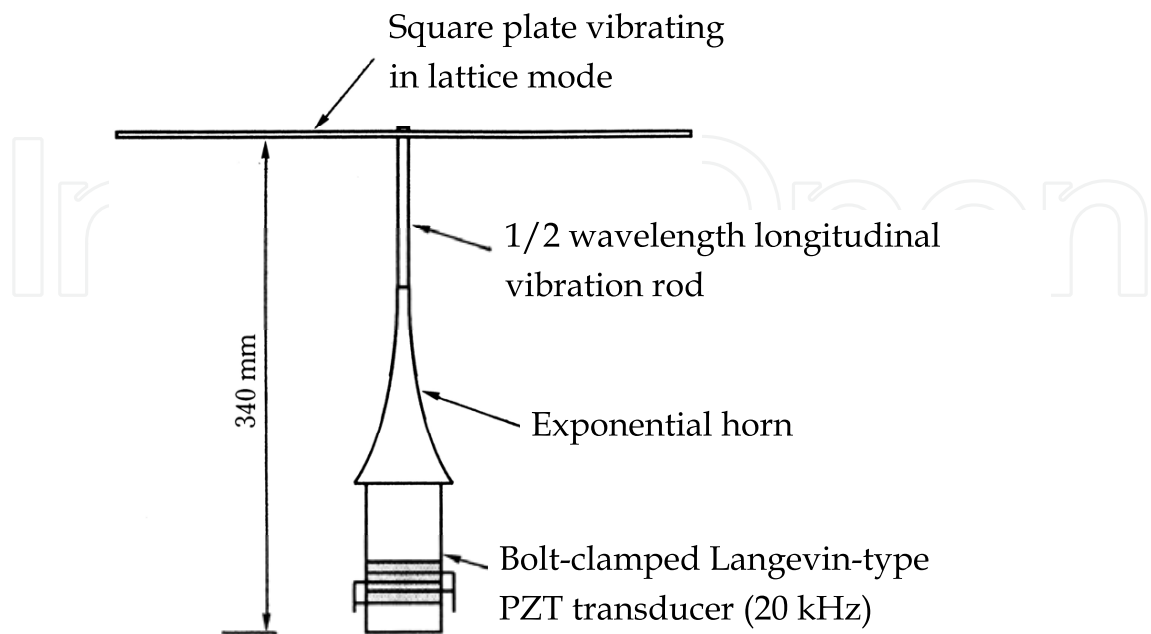

Fig. 1. Schematic diagram of an aerial ultrasonic source.

These parts are joined with screws. In general, transducers are required to generate longitudinal vibration with a frequency of approximately 20-100 kHz; I used a 20 kHz bolt-clamped Langevin-type piezoelectric (PZT) transducer (BLT transducer) to obtain large amplitudes. To increase the amplitude of the vibration of the transducer, an exponential horn (duralumin; diameter of thin end face, 10 mm; amplification rate, approximately was used. A rod (duralumin; diameter, 10 mm; length, 93 mm) was used to tune the resonant frequency of the 20 kHz longitudinal vibration of the transducer to that of the flexural vibration of the plate. The length of this rod should be an integral multiple of the half-wavelength of its longitudinal vibration; however, the rod can be omitted if not required. The flexurally vibrating plate attached at the end of the rod is allowed to vibrate by applying an amplified longitudinal vibration to the plate center as the driving point. Thus, lattice-mode vibration, in which the nodes of the flexural vibration are distributed in a lattice pattern, can be realized.

2.3 Design and fabrication of plate vibrating flexurally in the lattice mode

2.3.1 Design of vibrating plate

To distribute the nodes of a high-order flexural vibration in a lattice pattern by vibrating the center of a square plate, all sides of which undergo free vibration, high-order stripe-mode flexural vibration is induced between each pair of parallel sides of the plate, and the sum of the two flexural vibrations, which orthogonally intersect, is considered to be the lattice-mode flexural vibration. The equation used to design a plate vibrating flexurally in the stripe mode between opposite sides of the plate is given as

$$\lambda_t = \left\{ \frac{2\pi C_P h}{f} \right\}^{1/2} \tag{1}$$

where λ_t is the wavelength of the flexural vibration of the plate, C_P is a constant specific to the plate material, h is the thickness of the plate, and f is the frequency (Yamane et al., 1983). The length of the plate in the direction perpendicular to the striped pattern, L, is given by

$$L = (N - 0.5)\frac{\lambda_t}{2} \tag{2}$$

where N is the number of nodal lines and is even. When the plate is assumed to be a square of side L given by eq. (2), lattice-mode vibration can be obtained.

2.3.2 Vibration mode of plate

Figure 2 shows a schematic of a square flexurally vibrating plate viewed from above. When the center of the plate is assumed to be the origin and the x- and y-axes are set as shown in the figure, the vibration displacement at an arbitrary point (x,y) on the plate, ξ, is approximated using eq. (3) for $N \geq 10$.

$$\xi = \frac{\xi_0}{2}\left\{ \cos\frac{(N - 0.5)\pi x}{L} + \cos\frac{(N - 0.5)\pi y}{L} \right\} \tag{3}$$

Here, ξ_0 is the maximum vibration displacement.

The displacements of the plate flexurally vibrating in the stripe mode along the x- and y-directions are shown at the bottom and to the left of Fig. 2, respectively, and were calculated using eq. (3) assuming $N = 10$. Because the vibration mode is obtained by superimposing the vibration displacement in the x-direction (the first term in eq. (3)) onto that in the y-direction (the second term in eq. (3)), the nodal lines of the flexural vibration are represented by the broken lines in the figure. These nodal lines form a lattice pattern having an angle of 45° to each side of the plate. The number of nodal lines in each direction of the lattice mode is equal to N in the stripe mode. The interval between the lattice-mode nodal lines, ds, is given by

$$d_s = \frac{\lambda_t}{\sqrt{2}}$$ (4)

The antinodes of vibration displacement are positioned at the center of the regions surrounded by the nodal lines, and the displacements at adjacent antinodes have opposite phases (Miura, 1994).
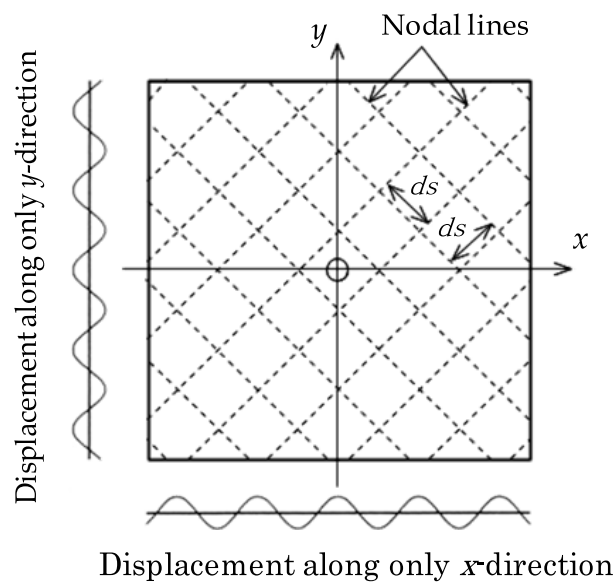

Fig. 2. Outline of a square plate vibrating in a lattice mode. Broken lines are nodal lines. ds is the interval of the lattice mode.

Thickness	Nodal number	Frequency	Wavelength of transverse	Width	Nodal interval of lattice-mode
h	N	f	vibration λ_t	L	d_s
[mm]		[kHz]	[mm]	[mm]	[mm]
1	10	19.89	22.4	106	15.8
2	10	20.64	30.7	146	21.7
3	10	20.45	37.3	177	26.4
5	10	19.71	48.2	229	34.1

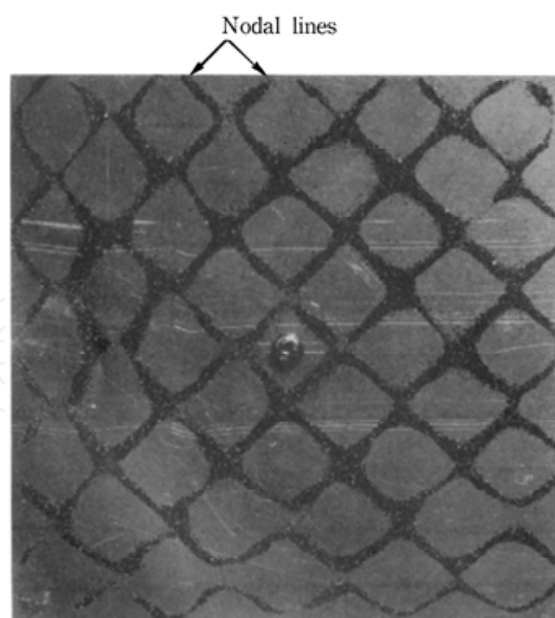Table 1. Details of the square plate vibrating in the lattice mode.

Fig. 3. Chladni sand figure showing nodal pattern of the square vibrating plate.

2.3.3 Fabrication of vibrating plate

Duralumin (JIS A2017P-T3; thickness h, 1-5 mm) was used to fabricate vibrating plates. The resonant frequency of the lattice mode vibration was approximately 20 kHz. The vibrating plates were designed using eqs. (1) and (2). Table 1 summarizes the details of the fabricated plates vibrating in a lattice mode when $N = 10$ and $h = 1, 2, 3$, or 5 mm.

2.3.4 Chladni sand figures

To determine the flexural vibration mode of each plate, Chladni sand figures were observed. Figure 3 shows the result for the plate with $h = 3$ mm (see Table 1). In the figure, the nodal lines on which sand particles (silicon carbide, #100) are concentrated are distributed in a lattice pattern similar to the nodal pattern (dotted lines) shown in Fig. 2. Vibrating plates with N not equal to 10 were also fabricated to observe the Chladni sand figures, and the vibration mode was confirmed to be the lattice mode with a different number of nodal lines.

2.4 Amplitude distribution of vibration displacement of plate

The vibration displacement at each position on the plate surface was measured using a noncontact microdisplacement meter to determine its distribution. The vibrating plate with $h = 3$ mm, which was used to obtain Fig. 3 (see Table 1), was used also for this measurement. The electric power input to the transducer was maintained at 1 W, and the square region indicated as (A) in Fig. 4 was targeted. Figure 5 shows the distribution of the normalized vibration displacement at various positions on the plate surface (using the center of the plate as the reference). The nodal lines of vibration displacement were distributed in a lattice pattern and the antinodes were positioned at the centers of the regions surrounded by the nodal lines, in good agreement with the schematic of the distribution of the vibration displacement within region (A) shown in Fig. 4, where the nodes are indicated by dashed lines.
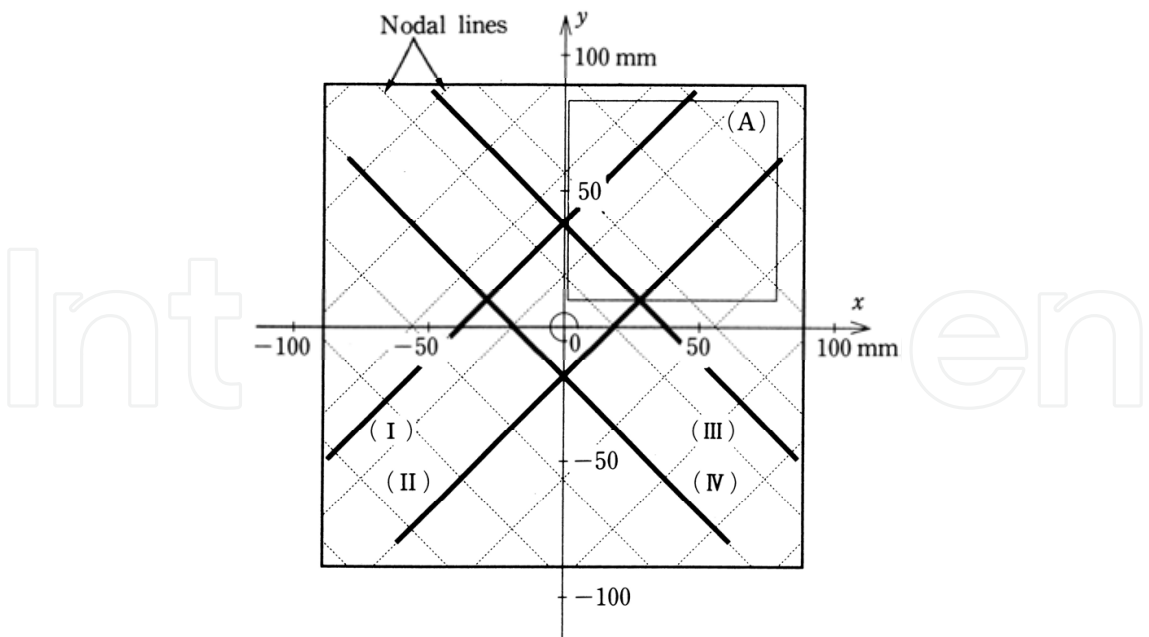
Fig. 4. Measurement positions of vibration displacement and sound pressure.
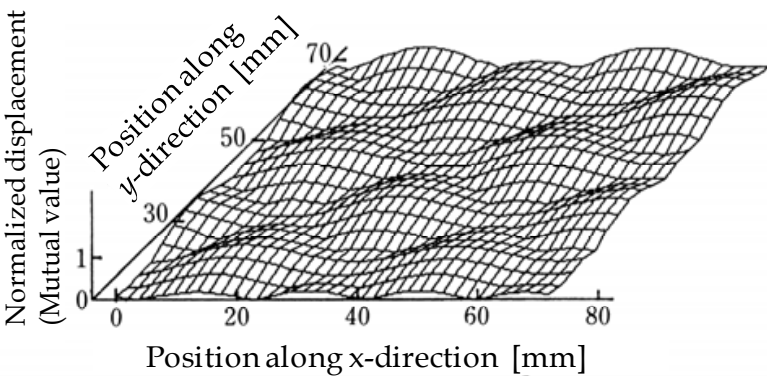

Fig. 5. Distribution of the vibration displacement.

2.5 Distribution of sound pressure near vibrating plate surface

To determine the distribution of sound pressure near the vibrating plate surface, the sound pressure at various positions approximately 1 mm above the plate along measurement lines (I)-(IV), indicated by bold lines in Fig. 4, was measured using condenser microphones (Bruel & Kjaer, 4138) while maintaining the input electric power at 1 W. Figure 6 shows the results, where the ordinate represents the normalized sound pressure and the abscissa represents the distance along each measurement line (using the foot of the perpendicular from the plate center to each measurement line as the reference). The distributions of sound pressure along measurement lines (I) and (III), which passed through antinodes of sound pressure, were similar to a sine wave with a specific amplitude and period. In this case, ds, the interval between adjacent nodes of sound pressure, was approximately 26 mm, in good agreement with the value of 26.4 mm calculated using eq. (4). In contrast, sound pressures along measurement lines (II) and (IV), which were located on the nodal lines, were low.

2.6 Directivity of sound waves in remote acoustic fields

In this section, I theoretically and experimentally examine the directivity of the sound waves radiated from the plate vibrating in the lattice mode into remote acoustic fields.

2.6.1 Method of calculating directivity

The directivity of the sound waves radiated from the square plate vibrating in the lattice mode into remote acoustic fields is calculated as follows.

As shown in Fig. 7, it is assumed that the distance from the plate center to a sufficiently remote observation point P is R_0 and that the distance from an arbitrary point (x,y) on the
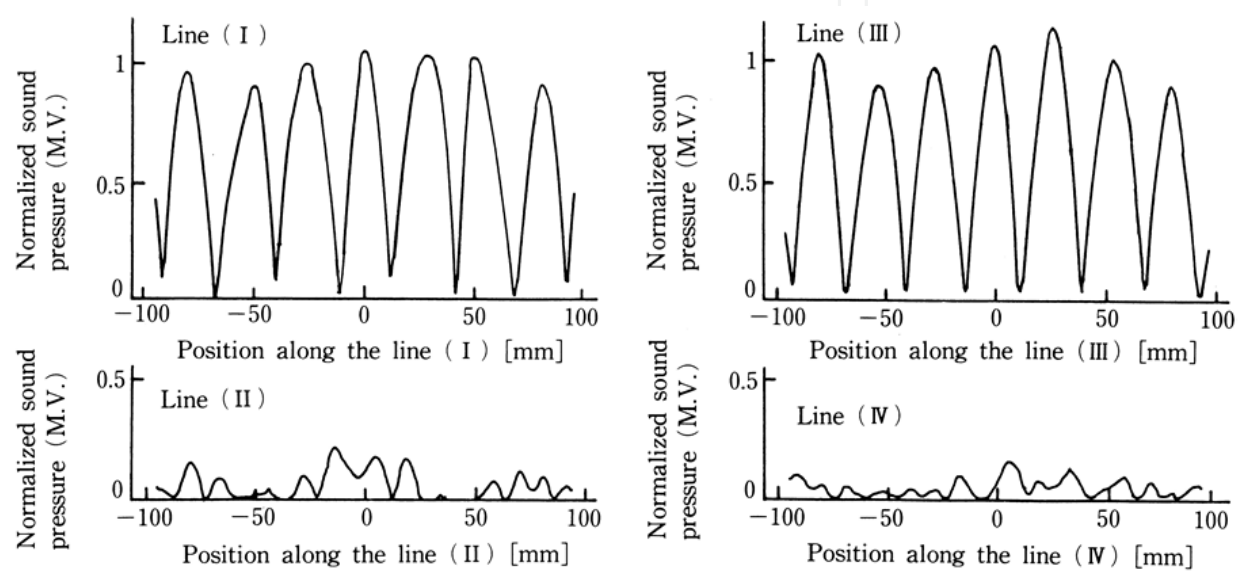

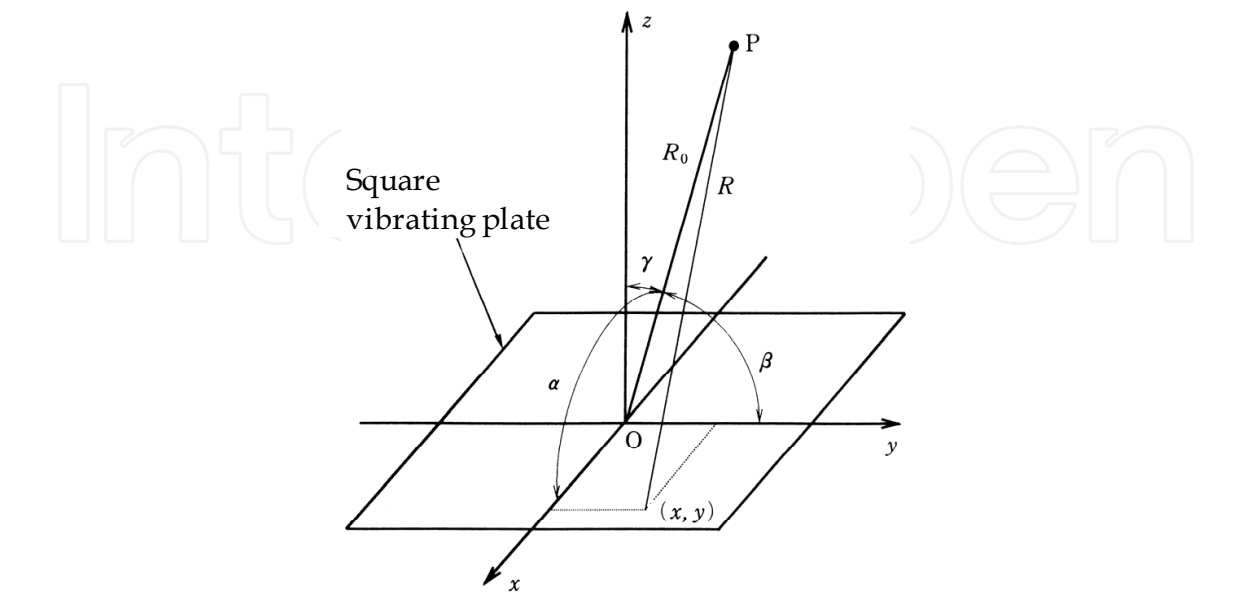Fig. 6. Distributions of the sound pressure near the vibrating plate. Lines (I) - (IV) are indicated in Fig.4.

Fig. 7. Coordinate system for the evaluating directivity of radiated sound waves.

plate surface to P is R. When the angles between OP and the x-, y-, and z-axes are assumed to be α, β, and γ, respectively, R is given by

$$R = R_0 - (x\cos\alpha + y\cos\beta) \tag{5}$$

Therefore, the component of the volume velocity over a small area $dxdy$ in the OP direction is $\xi dxdy\cos\gamma$, and the velocity potential $d\Phi$ at P is given by

$$d\Phi = \frac{\xi dxdy}{2\pi R}\cos\gamma \, e^{j(\omega t - kR)} \tag{6}$$

where ω is the angular frequency and k is the wavelength constant of sound waves. When P is sufficiently remote from the plate center, $R_0 \gg x\cos\alpha + y\cos\beta$. When assuming that R only affects the phase difference of the velocity potential Φ, Φ at P is obtained by integrating eq. (6) over the entire plate area.

$$\Phi = \frac{\cos\gamma}{2\pi R_0} \int\limits_{-\frac{L}{2}}^{\frac{L}{2}} \int\limits_{-\frac{L}{2}}^{\frac{L}{2}} \xi e^{j(\omega t - kR)} dxdy \tag{7}$$

The sound pressure p at P is expressed by

$$p = \rho\frac{\partial\Phi}{\partial t} \tag{8}$$

where ρ is the density of air. By substituting eq. (7) into eq. (8),

$$p = \frac{\omega\rho\xi_0\cos\gamma}{2\pi R_0}\left(\frac{A\sin\frac{k_\beta L}{2}}{k_\beta} + \frac{B\sin\frac{k_\alpha L}{2}}{k_\alpha}\right) \cdot e^{j(\omega t - kR_0 + \frac{\pi}{2})} \tag{9}$$

is obtained. Here, A, B, k_α, k_β, and k_N are given as follows.

$$A = \frac{1}{k_\alpha + k_N}\sin\frac{(k_\alpha + k_N)L}{2} + \frac{1}{k_\alpha - k_N}\sin\frac{(k_\alpha - k_N)L}{2}$$

$$B = \frac{1}{k_\beta + k_N}\sin\frac{(k_\beta + k_N)L}{2} + \frac{1}{k_\beta - k_N}\sin\frac{(k_\beta - k_N)L}{2}$$

$$k_\alpha = k\cos\alpha \, , \quad k_\beta = k\cos\beta$$

$$k_N = \frac{(N - 0.5)\pi}{L}$$

2.6.2 Method of measuring directivity

The sound pressure at a distance of 1.8 m from the plate center was experimentally measured using a 6.4-mm-diameter condenser microphone (B&K 4136) while maintaining the electric power input to the acoustic source at 1 W.

The characteristics of the vibrating plates used in the experiment are summarized in Table 1. No baffles were used because the dimensions of the vibrating plates were sufficiently greater than the wavelength of the sound waves and baffles were considered to have little effect. The back of the vibrating plates was covered with glass wool with a thickness of 50 mm to absorb the sound waves radiated from the back. The measurement distance was set at values greater than the Fresnel last maximum (at which the phase difference due to differences in the distance from the vibrating plate surface is negligible and a remote acoustic field is assumed to be formed) on the centerline of a disc piston with a diameter equal to the length of the diagonal of the vibrating plates (David & Cheeke, 2002).
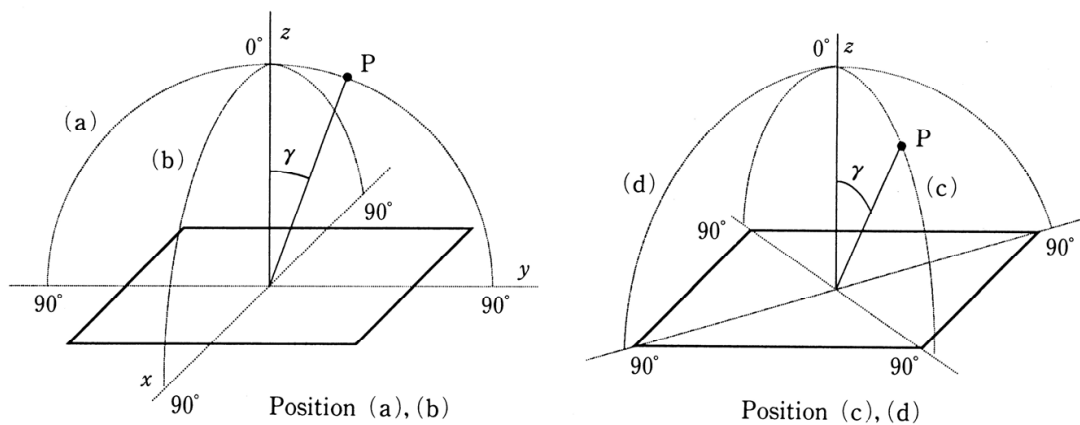

Fig. 8. Measurement positions of directivity.

2.6.3 Directivity in various directions

First, sound pressures in various directions were measured using the vibrating plate with h = 3 mm and N = 10 (see Table 1) for different angles between OP and the z-axis, γ, from -90 (x-y plane), 0 (z-axis), to 90° (x-y plane) to examine the radiation direction of the sound waves. Figure 8 shows the measurement positions: (a) γ = -90 $-$ 90° in the y-z plane (α = 90°), (b) γ = -90 $-$ 90° in the x-z plane (β = 90°), (c) γ = -90 $-$ 90° in the y = x and z–axis plane (α = β), and (d) γ = -90 $-$ 90° in the y = -x and z–axis plane. The measurement results are shown by the solid lines in Figs. 9(a)$-$9(d). The abscissa represents γ and the ordinate represents the normalized sound pressure. In Figs. 9(a) and 9(b), sharp main lobes of the radiated sound waves are observed in two directions; they have specific z–axis-symmetric angles in the y-z and x-z planes, respectively. However, no sharp main lobes are observed in the y = x and z–axis plane and the y = -x and z–axis plane, as shown in Figs. 9(c) and 9(d), respectively. The dashed lines in Figs. 9(a)$-$9(d) represent the calculation results obtained using eq. (9), and are in good agreement with the experimental results in all cases.

The directions of the main lobe are symmetric about the z-axis and the angle between the z-axis and the main lobe, γ_{m}, is given by

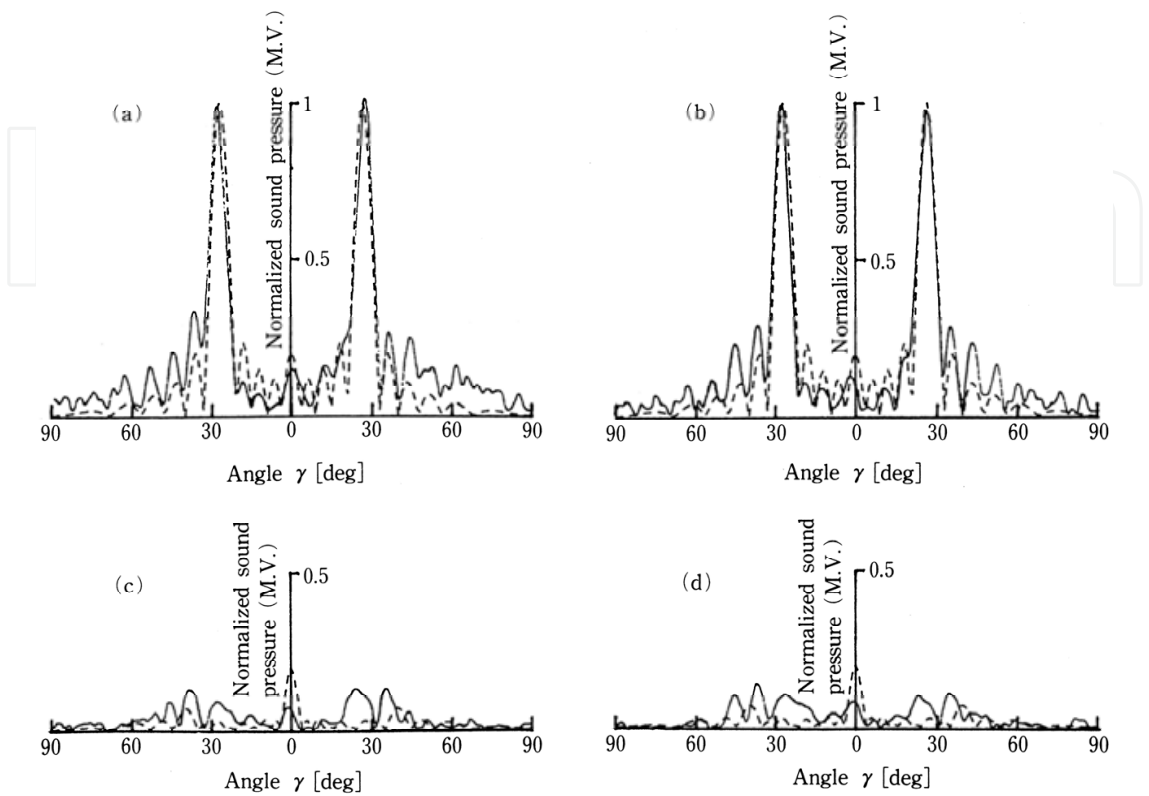$$\gamma_m = \sin^{-1} \frac{\lambda_a}{\lambda_t} \qquad (10)$$

Fig. 9. Directivity patterns in various directions. ------ : Experimental, - - - : calculated.
Position (a) is in the y-z axis plane, (b) is in the x-z axis plane, (c) is in the y=x and the z-axis plane, (d) is in the y= - x and the z-axis plane.
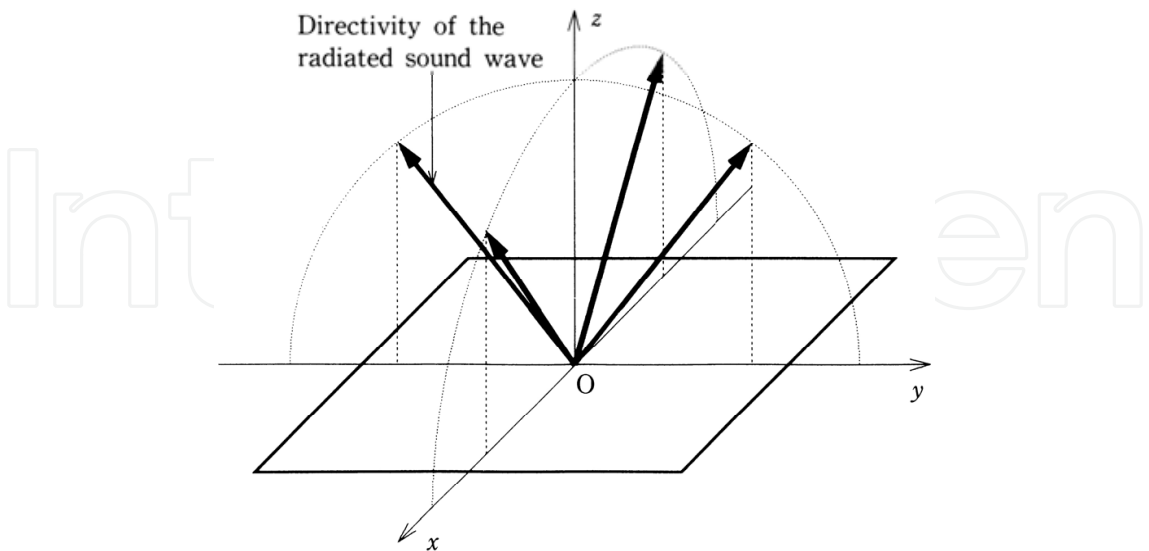

Fig. 10. Outline of the directivity.

where λa is the wavelength of the sound waves in air. The measurement results in Figs. 9(a) and 9(b) reveal that γ_m = 27.2°, which is in good agreement with the value of 27.0° calculated

using eq. (10). When similar experiments were carried out for planes other than the above-mentioned planes, the sound pressures were low, similarly to the cases in Figs. 9(c) and 9(d). Therefore, the sound waves radiated from the plate vibrating in the lattice mode have main lobes only in four symmetric directions with a specific angle from the z-axis in the y-z and x-z planes, as shown in Fig. 10.
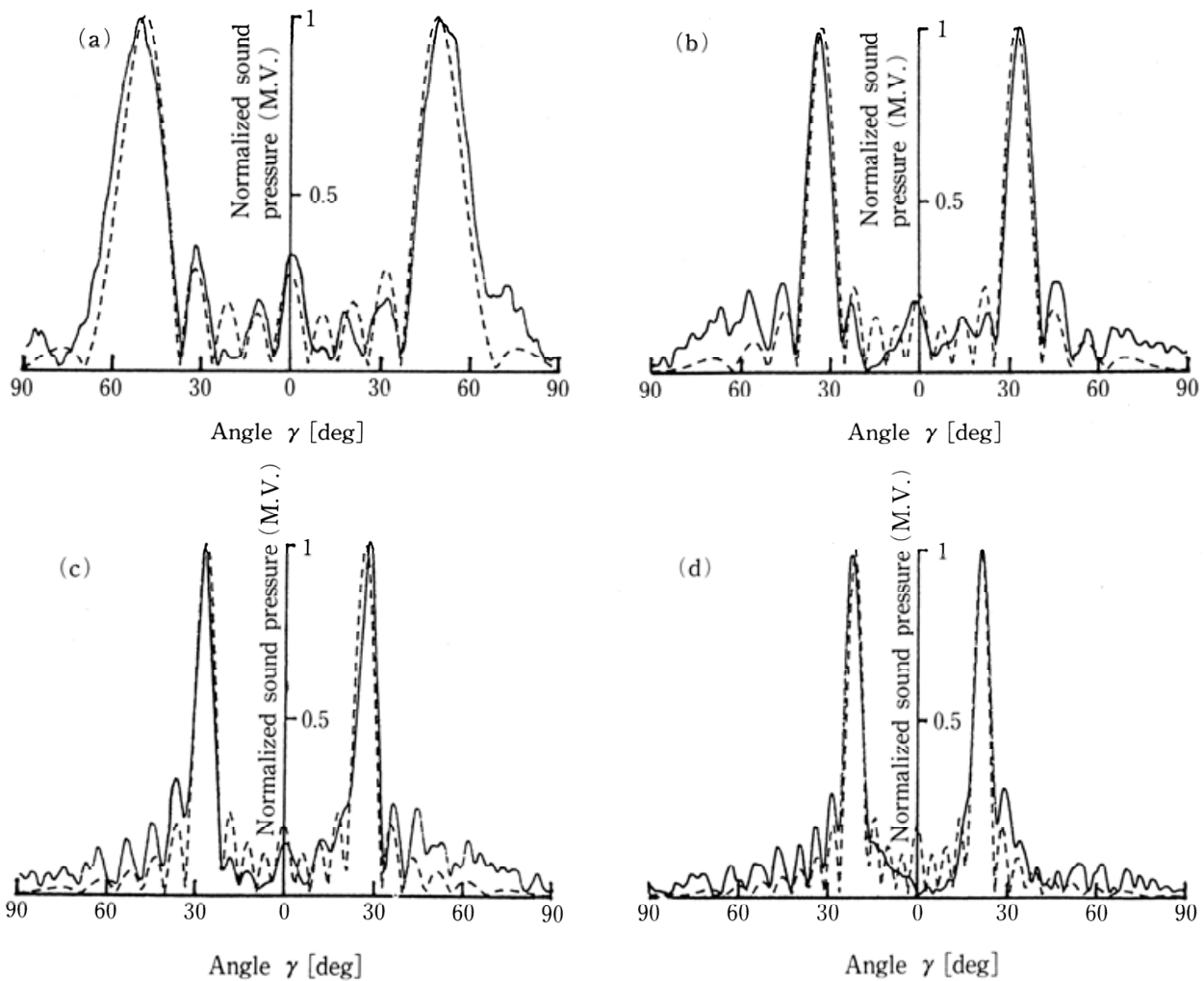

Fig. 11. Directivity patterns for various λ_t/λ_a. ----- : Experimental, - - - : calculated. (a) changing $\lambda_t/\lambda_a = 1.29$ ($h=1$ mm), (b) $\lambda_t/\lambda_a = 1.83$ ($h=2$ mm), (c) $\lambda_t/\lambda_a = 2.20$ ($h=3$ mm), (d) $\lambda_t/\lambda_a = 2.74$ ($h=5$ mm).

Thickness	Nodal interval of lattice-mode	$\dfrac{\lambda_t}{\lambda_a}$	Angle from z-axis to main lobe γ_m [deg]		Angle width of half value [deg]	
h [mm]	d_s [mm]		Calculated value	Experimental value	Calculated value	Experimental value
1	15.8	1.29	51.1	50.2	19.2	19.6
2	21.7	1.83	33.2	33.7	10.0	9.8
3	26.4	2.20	27.0	27.2	7.8	7.8
5	34.1	2.74	21.4	21.4	6.0	6.4

Table 2. Directivity of the square plate vibrating in the lattice mode.

2.6.4 Directivities for different wavelengths of flexural vibration of plate

Next, to examine the directivity for different wavelengths (λ_t) of the flexural vibration of the plate, the sound pressure on the y-z plane ($a = 90°$, the case of (a) in Fig. 8), on which main lobes were observed, was measured by changing γ from -90 to 90° for the vibrating plates with a constant frequency with $N = 10$ and h in the range of 1-5 mm (see Table 1). The measurement results are shown by the solid lines in Fig. 11: (a) $\lambda_t/\lambda_a = 1.29$ ($h = 1$ mm), (b) $\lambda_t/\lambda_a = 1.83$ ($h = 2$ mm), (c) $\lambda_t/\lambda_a = 2.20$ ($h = 3$ mm), and (d) $\lambda_t/\lambda_a = 2.74$ ($h = 5$ mm). The ordinate and abscissa are the same as those in Fig. 9(a). From Figs. 11(a)−11(d), it is found that the radiated sound waves have main lobes in two directions and that their directions are symmetric about the z-axis with an angle depending on λ_t/λ_a, similarly to the cases in Figs. 9(a) and 9(b). The dashed lines in Fig. 11 represent the calculation results obtained using eq. (9), and are in good agreement with the experimental results.

As shown in Table 2, γ_m decreased when λ_t/λ_a increased, i.e., when h, and thereby the wavelength of flexural vibration, increased. The experimental and calculated values of γ_m were in good agreement.

Moreover, the angle range of full-width half-maximum of the sound pressure was compared among the main lobes, as shown in the rightmost column in Table 2. This angle range decreased with increasing λ_t/λ_a, indicating that the directivity became sharp.

2.7 Summary

The details of the aerial ultrasonic source with a square plate vibrating in the lattice mode described in this section are summarized as follows.

1. A practical method for designing the flexurally vibrating plate was proposed.
2. The angle between the nodal lines of the lattice-mode vibration and the sides of the plate was 45°.
3. The calculation results for the distributions of the vibration displacement of the plate were confirmed by measuring the distributions of vibration displacement and sound pressure near the plate surface.
4. Regarding the directivity of the plate vibrating in a lattice mode, the theoretical values calculated using eq. (9) and the experimental values for the fabricated plates were in good agreement.
5. The sound waves that were radiated from the vibrating plate had sharp main lobes in four symmetric directions on the y-z and x-z planes, with a specific angle from the z-axis.
6. The angle between the z-axis and the main lobe, γ_m, decreased when λ_t/λ_a increased, i.e., when h, and thereby the wavelength of flexural vibration, increased.
7. The angle range of the main lobe in which the sound pressure was half the maximum value decreased with increasing λ_t/λ_a, indicating that the directivity became sharp.

3. Removal of unnecessary gas by intense aerial ultrasonic source

3.1 Outline

In this section, I discuss the effect of the intense aerial ultrasonic source described in section 2 on enhancing the removal of an unnecessary gas from air. In previous studies, We

examined the effect of the combined use of aerial ultrasonic waves with water mist on the removal of a gas, with the aim of applying it to the removal of an unnecessary gas. As a result, we found that both aerial ultrasonic waves and water mist are necessary to remove a low-hydrophilicity lemon-odor gas and that the maximum removal percentage reached approximately 40%, (Miura, 2007a).

In this method, intense ultrasonic waves are propagated into air from the acoustic source using the square plate flexurally vibrating in the lattice mode, and water is added dropwise onto the positions of the antinodes of flexural vibration on the plate to generate a mist of water microparticles. Ultrasonic waves are irradiated onto the water microparticles and a gas to enhance the absorption of the gas by the water microparticles. The flexurally vibrating plate has two roles: the radiation of sound waves and the formation of water microparticles. The frequency of collisions between microparticles and gas molecules increases because of differences in the velocity of particles in the sound waves and in their momentum owing to differences in their size, enhancing the aggregation and settlement of water microparticles and gas molecules.

To further increase the removal efficiency for a low-hydrophilicity gas, water mist of small particles (average particle diameter, approximately 3 μm) generated using a water spray system was used, as well as water mist of large particles (average particle diameter, approximately 60 μm) formed by the flexural vibration of the plate. The gas removal efficiency achieved when aerial ultrasonic waves are irradiated onto these water particles is discussed. Here, the particle diameter was calculated using Lang's equation (Lang, 1962).

In this section, I describe the process of the removal of a gas by applying water mist of small particles when intense standing-wave acoustic fields were formed within a gas removal chamber. Also, I discuss the gas removal efficiency achieved upon changing the amounts of the water mist of large and small particles, the electric power input to the transducer, and the initial gas concentration.

Although a toxic gas such as dioxin could be used as the gas to be removed, a gas harmless to humans should be used because the experiments were carried out in a simple laboratory. The gas also was required to have low hydrophilicity so as not to easily aggregate in water and be usable at normal temperatures and pressures, and its gas concentration was required to be easily measurable. To satisfy these conditions, a gas evaporated from lemon oil (Sigma-Aldrich Corporation; Product No., W262528; chemical formula, $C_{10}H_{16}O$; specific gravity, 0.855) was used.

3.2 Gas removal apparatus

In this section, I give an outline of the gas removal apparatus used in the experiment.

3.2.1 Outline of apparatus

Figure 12 shows a schematic of the experimental setup. The gas removal apparatus used in this experiment consists of a supply fan with an activated carbon filter (amount, 92 cm^3/s), a unit for generating the lemon-odor gas, a digital constant-rate pump for supplying water to the vibrating plate, a water spray system for generating water mist of small particles, an

acoustic source mainly comprising a 20 kHz BLT transducer and a square plate vibrating flexurally in the lattice mode, an acrylic chamber as the main body, and an exhaust fan for removing air passing through the chamber. The flexurally vibrating plate of the acoustic source, 36 narrow hypodermic needles that supply water to the vibrating plate to form water mist of large particles, and reflective boards used to form standing-wave acoustic fields are included in the acrylic chamber. The digital constant-rate pump is used to supply water at a constant rate to the vibrating plate within the acrylic chamber. In addition, a 2.4 MHz ultrasonic humidifier equipped with a water spray system is used to generate water mist of small particles.
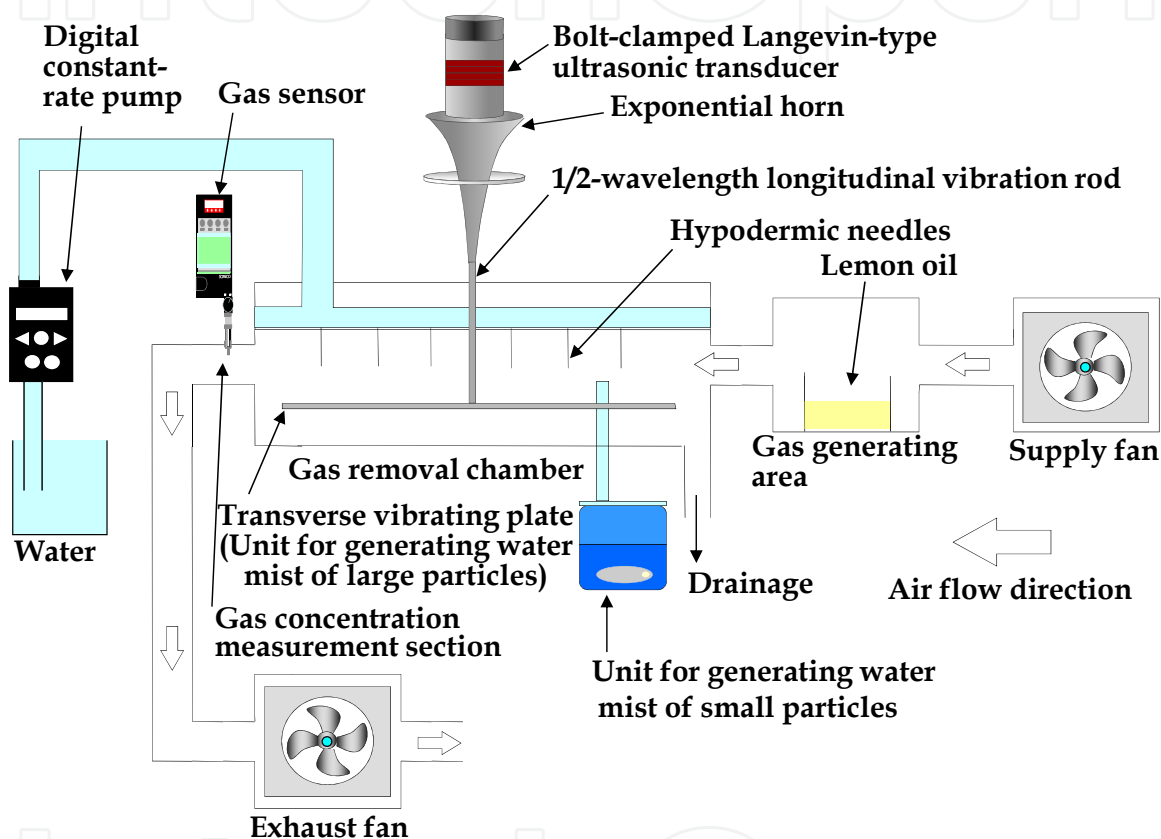

Fig. 12. Schematic of gas removal apparatus.

To measure the gas concentration, a hot-wire semiconductor-type gas sensor is attached to the pipe that connects the acrylic chamber to the exhaust fan.

3.2.2 Aerial ultrasonic source used in experiment

Figure 13 shows a schematic of the ultrasonic source used in the experiment. As shown in the figure, an exponential horn (diameter of thick end face, 70 mm; diameter of thin end face, 10 mm; length, 150 mm; amplification rate, 7.0) and a half-wavelength longitudinal vibration rod (diameter, 10 mm; length, 116 mm) were connected to a 20 kHz BLT transducer (D45520). A duralumin square plate vibrating flexurally in the lattice mode (plate constant, $C_P = 1.51 \times 10^6$ Hz·mm; $N = 12$; $h = 3$ mm; $L = 217$ mm; resonant frequency, 19.8 kHz) was screwed onto the end of the rod.

Bolt-clamped Langevin-type
ultrasonic transducer

Exponential horn
Thick end face 70 mm
Thin end face 9 mm

Transverse vibrating plate
Square of side 217 mm
Thickness 3 mm
Resonance frequency 19.8 kHz

1/2-wavelength longitudinal
vibration rod
Diameter 10 mm
Length 116 mm

Fig. 13. Schematic of ultrasonic transducer.

Bolt-clamped Langevin-type
ultrasonic transducer

Exponential horn

1/2-wavelength longitudinal
vibration rod

42 mm

14 mm

Upper reflective board

Transverse
vibrating plate

Lower reflective
board

Fig. 14. Positions of reflective boards.

3.2.3 Distances between flexurally vibrating plate and reflective boards

Planar reflective boards were installed above and below the vibrating plate to form an intense standing-wave acoustic field within the acrylic chamber, as shown in Fig. 14.

The relationship between the velocity c and wavelength λ_a of the sound waves radiated from the vibrating plate into free space is as follows.

$$\lambda_a = \frac{c}{f} \tag{11}$$

Here, $c = 331.5 + 0.6t$ (temperature (t) = 25 °C) and f is the frequency. The wavelength of the sound waves transmitted in the vertical direction, λ_y, is given by

$$\lambda_y = \frac{\lambda_a}{\sin \theta} \tag{12}$$

where θ is the radiation angle. Assuming the wavelength of the flexural vibration of the plate to be λ_t, θ is expressed by

$$\theta = \cos^{-1}\left(\frac{\lambda_a}{\lambda_t} \right) \tag{13}$$

To form standing waves between the vibrating plate and the upper reflective board, the distance between them, W, must be set at an integral multiple of the half-wavelength of the sound waves transmitted in the vertical direction and is given as follows.

$$W = \frac{\lambda_y}{2} n \ (n \text{ is an arbitrary integer}) \tag{14}$$

Here, W is set to 42 mm, which is double the wavelength of the sound waves transmitted in the vertical direction. In this case, the electric impedance of the transducer is maximized. The distance between the vibrating plate and the lower reflective board is set to 14 mm, at which the electric impedance of the transducer is minimized.
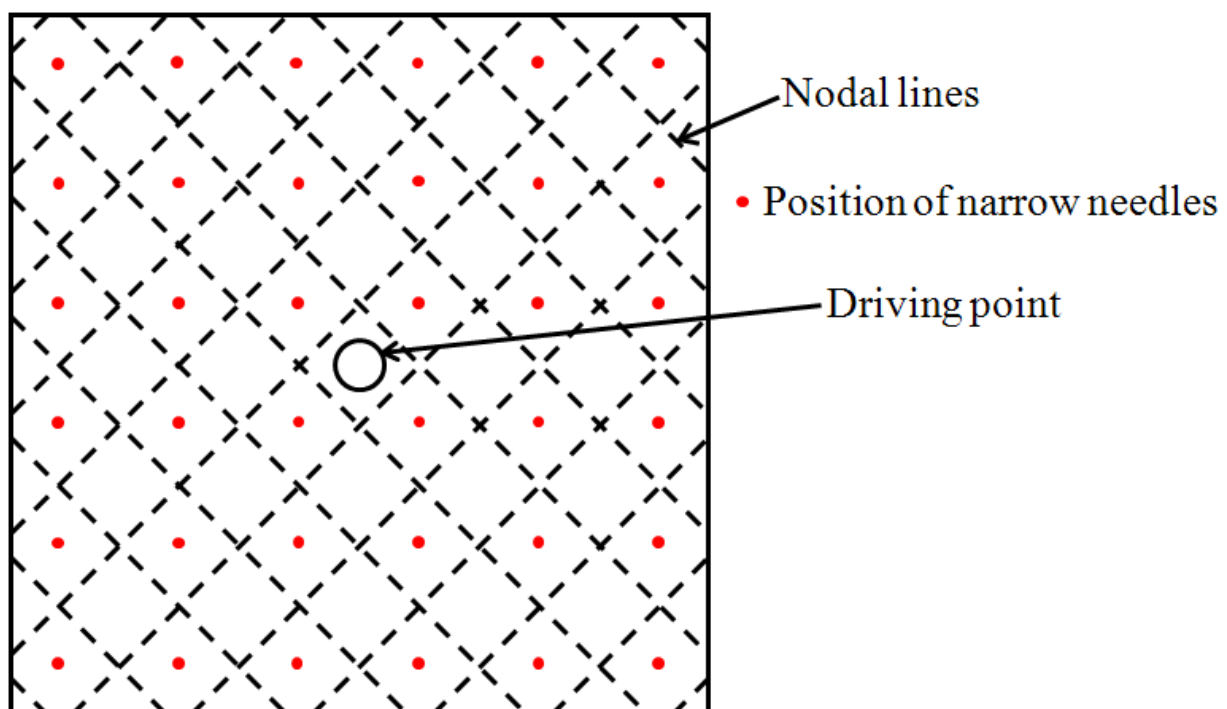

Fig. 15. Positions of narrow needles.

3.2.4 Position of narrow needles

In the experiment, water mist to absorb the gas was generated by supplying water to the vibrating plate. Figure 15 shows the positions of the narrow hypodermic needles installed to supply water to the vibrating plate. The dashed lines in the figure represent nodal lines of vibration. Thirty-six narrow needles are positioned exactly above the antinodes at the centers of the regions surrounded by the nodal lines.

3.3 Effect of combined use of aerial ultrasonic waves and water mist on removal of unnecessary gas

In this section, on the basis of experimental results, We examine the effects of using intense aerial ultrasonic waves and two types of water mist of particles with different diameters on the removal of an unnecessary gas.

3.3.1 Gas removal process

The process for removing the lemon-odor gas by irradiating aerial ultrasonic waves was examined in the presence and absence of water mist of large and small particles.
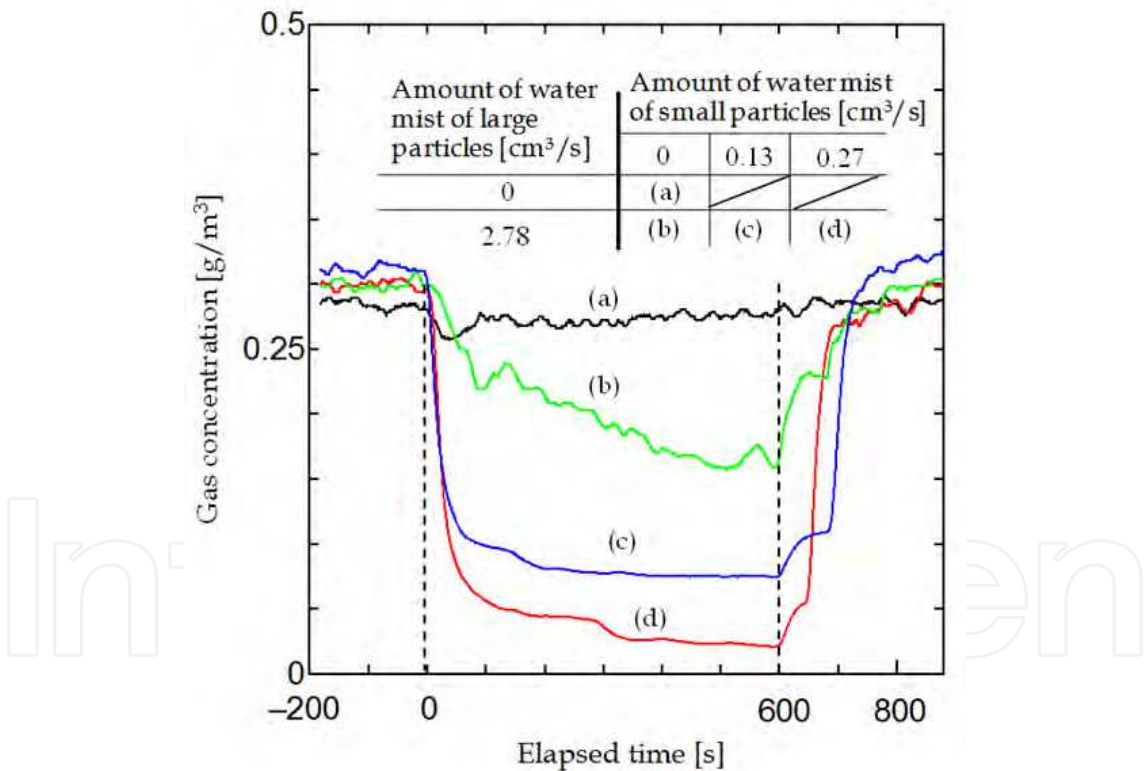

Fig. 16. Gas removal process. The input electric power is 50 W and the driving frequency is 19.8 kHz.

Because the rate of vaporization of the generated gas was unstable when the fan started operating, the apparatus was left to stand for approximately 180 s to stabilize the rate of generation of the gas. The time at which the vaporization rate was stabilized was assigned a time of -180 s, and the apparatus was left to stand for another 180 s. The electric power was

input to the ultrasonic source at a time of 0 s to generate ultrasonic waves in air. Simultaneously, water was supplied to the vibrating plate through the narrow needles attached to the upper reflective board, and water mist was formed by vibrating the plate. Moreover, water mist of small particles was also generated by the water spray system. This condition was maintained for 600 s. Then, the generation of the ultrasonic waves and water mist was stopped, and the state within the acrylic chamber was observed.

The experimental conditions were as follows: the input electric power was maintained at 50 W, the driving frequency was 19.8 kHz, the amount of water mist of large particles was 0 or 2.78 cm^3/s, and the amount of water mist of small particles was 0, 0.13, or 0.27 cm^3/s. Figure 16 shows the experimental results, where the ordinate represents the concentration of lemon-odor gas and the abscissa represents the elapsed time. When no mist was generated, case of (a), the gas concentration negligibly decreased during the measurement time from 0 to 600 s (with ultrasonic irradiation). When the amounts of water mist of large and small particles were 2.78 and 0 cm^3/s, respectively, case of (b), the gas concentration decreased slightly. However, when the amount of water mist of small particles was increased to 0.13, case of (c), and 0.27 $cm3$/s, case of (d), the gas concentration sharply decreased after the start of ultrasonic irradiation, maintained an almost constant value, then increased to the initial value shortly after the end of ultrasonic irradiation (600 s). The results for water mist of small particles in the absence of water mist of large particles are not show, since aggregation and drainage did not occurred in this case. Therefore, the gas was effectively removed by the combined use of ultrasonic waves and the water mist of both large and small particles.
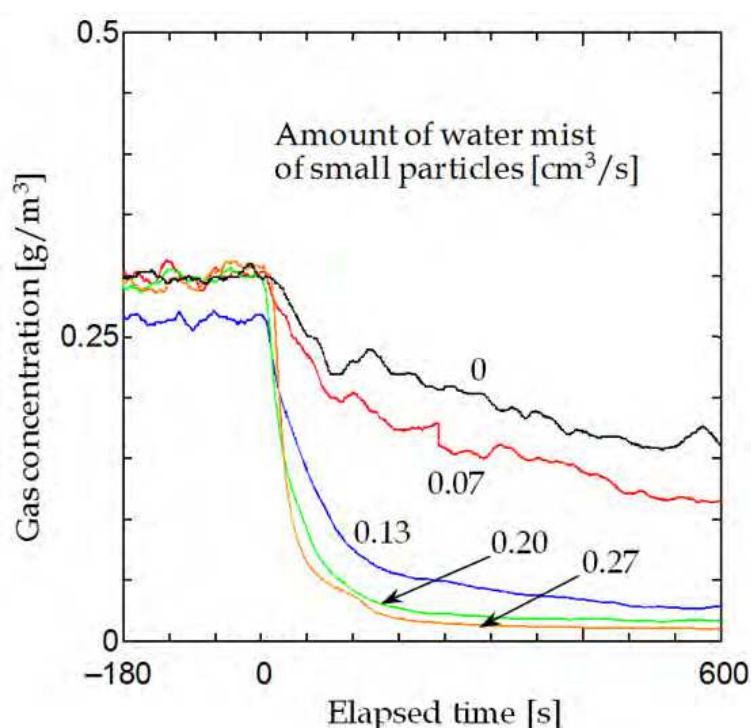

Fig. 17. Relationship between elapsed time and gas concentration. The input electric power is 50 W, the amount of water mist of large particles is 2.78 cm^3/s, and the driving frequency is 19.8 kHz.

3.3.2 Gas removal efficiency with different amounts of water mist of small particles

To examine the gas removal efficiency with different amounts of the water mist of small particles, a gas removal experiment was carried out with the electric power input to the transducer fixed at 50 W and the amount of water mist of large particles maintained at 2.78 cm^3/s while the amount of water mist of small particles was set at 0, 0.07, 0.13, 0.20, or 0.27 cm^3/s. The experimental procedure followed was that described in sec. 3.3.1.

Figure 17 shows the experimental results, where the ordinate represents the concentration of lemon-odor gas and the abscissa represents the elapsed time, with the amount of water mist of small particles as a parameter. In all cases, the gas concentration changed negligibly between -180 and 0 s, during which no ultrasonic waves were irradiated. When ultrasonic waves and the water mist were generated at 0 s, however, the gas concentration sharply decreased.
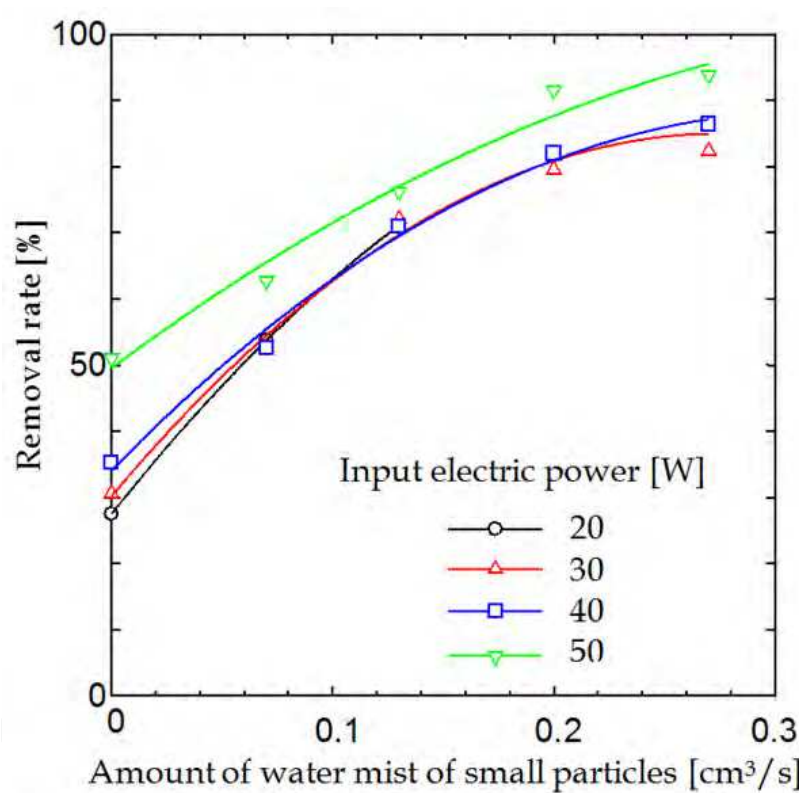

Fig. 18. Relationship between amount of water mist of small particles and removal rate. The amount of water mist of large particles is 2.78 cm^3/s, and the driving frequency is 19.8 kHz.

3.3.3 Gas removal rate with different amounts of water mist of small particles

Similar experiments were also performed for input electric powers of 20, 30, and 40 W as well as above 50 W. The gas removal rate Px was defined as the index describing the removal rate of gas.

$$Px = \frac{G_a - G_b}{G_a} \tag{15}$$

Here, G_a and G_b are the average concentrations of lemon-odor gas [g/m³] between -180 and 0 s and between 500 and 600 s, respectively. Equation (15) indicates that the greater the value of Px, the higher the gas removal rate.

Figure 18 shows the experimental results, where the ordinate represents the gas removal rate and the abscissa represents the amount of water mist of small particles, with the electric power input to the transducer as a parameter. When the amount of water mist of large particles was constant, the gas removal rate increased with the amount of water mist of small particles; however, no marked difference in the gas removal rate was observed within the range of input electric power examined in this experiment. The gas removal rate reached approximately 90% when the amount of water mist of small particles was 0.27 cm³/s and the input electric power was 50 W. Moreover, the gas was removed when the amount of water mist of small particles was 0 cm³/s, i.e., when only water mist of large particles was used; in this case, the gas removal rate reached approximately 60% when the input electric power was 50 W. These results indicate that most of the gas can be removed by using water mist of both large and small particles.
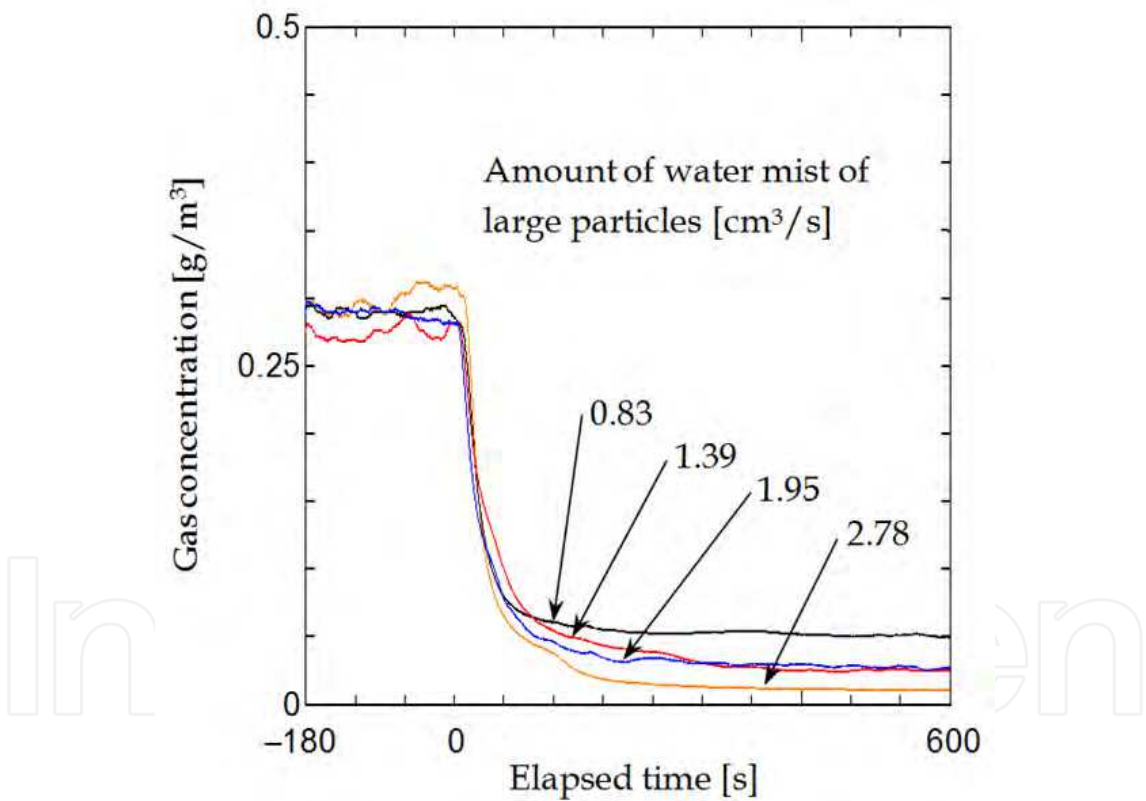

Fig. 19. Relationship between elapsed time and gas concentration. The input electric power is 50 W, the amount of water mist of small particles is 0.27 cm³/s, and the driving frequency is 19.8 kHz.

3.3.4 Gas removal rate with different amounts of water mist of large particles

To examine the gas removal efficiency with different amounts of water mist of large particles, a gas removal experiment was carried out with the electric power input to the

transducer fixed at 50 W and the amount of water mist of small particles maintained at 0.27 cm^3/s while the amount of water mist of large particles was set at 0.83, 1.39, 1.95, or 2.78 cm^3/s. The experimental procedure followed was that described in sec. 3.3.1.

Figure 19 shows the experimental results, where the ordinate represents the concentration of lemon-odor gas and the abscissa represents the elapsed time, with the amount of water mist of large particles as a parameter. In all cases, the gas concentration changed negligibly between -180 and 0 s, during which no ultrasonic waves were irradiated. When ultrasonic waves and the water mist were generated at 0 s, however, the gas concentration sharply decreased and reached a constant value after approximately 200 s.

Next, similar experiments were performed for input electric powers of 30 and 40 as well as 50 W, to obtain the gas removal rate. The gas removal rate was then calculated using eq. (15).

Figure 20 shows the experimental results, where the ordinate represents the gas removal rate and the abscissa represents the amount of water mist of large particles, with the input electric power as a parameter. When the input electric power was in the range examined in this experiment and the amount of water mist of small particles was constant, the gas removal rate tended to increase as the amount of water mist of large particles and the input electric power increased.
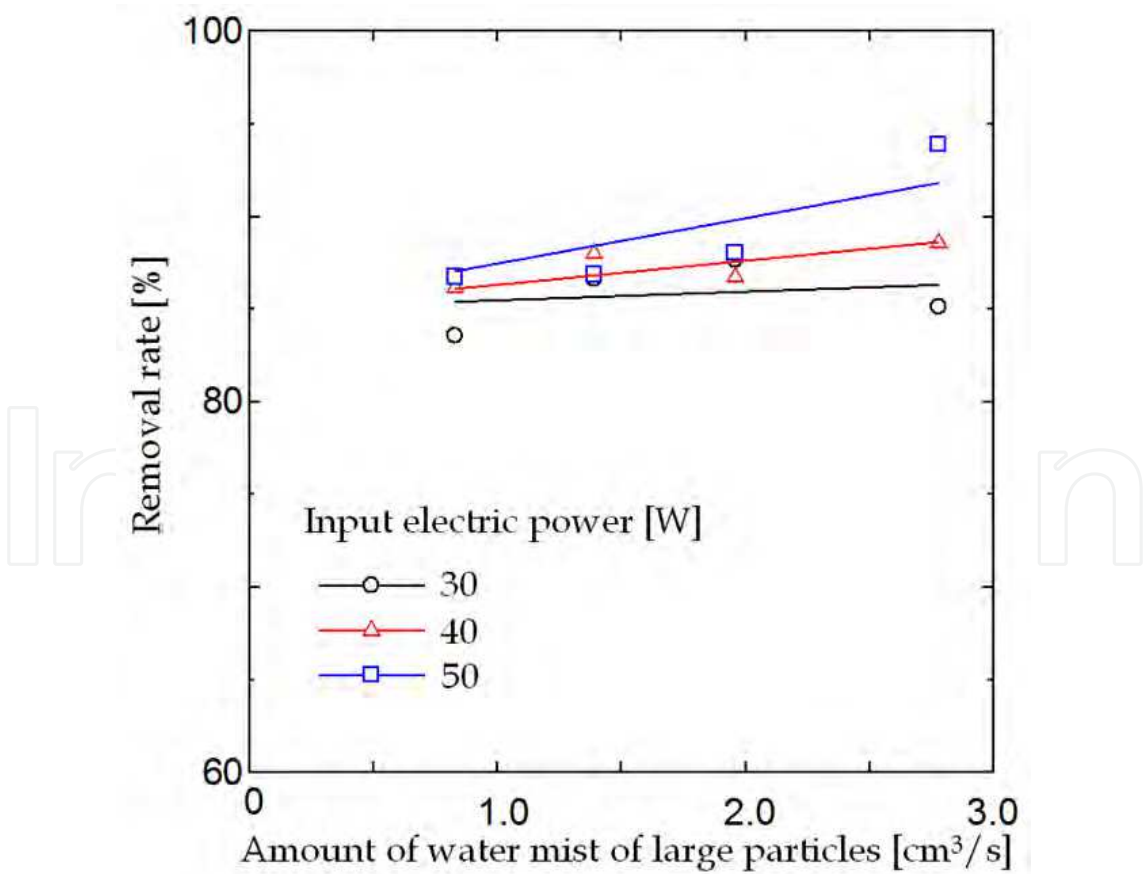

Fig. 20. Relationship between amount of water mist of large particles and removal rate. The Amount of water mist of small particles is 0.27 cm^3/s, and the driving frequency is 19.8 kHz.

3.3.5 Examination of gas removal efficiency with different initial gas concentrations

To examine the gas removal efficiency with different initial concentrations of lemon-odor gas, a gas removal experiment was performed. In this experiment, the area of the base of the petri dish into which the lemon oil was placed was changed to vary the amount of generated gas. The experimental procedure was the same as before.

Figure 21 shows the experimental results, where the ordinate represents the concentration of lemon-odor gas and the abscissa represents the elapsed time, with the initial gas concentration as a parameter. In all cases, the gas concentration remained almost constant between -180 and 0 s, during which no ultrasonic waves were irradiated. When ultrasonic waves and the water mist were generated at 0 s, however, the gas concentration sharply decreased.

Next, a similar experiment was carried out to obtain the gas removal rate with different initial gas concentrations. The gas removal rate was calculated from the experimental results using eq. (15). Figure 22 shows the results, where the ordinate represents the gas removal rate and the abscissa represents the initial gas concentration. When the amounts of water mist of small and large particles and the input electric power were constant, the gas removal rate tended to increase with the initial gas concentration in the range examined in this experiment. This was considered to be because the higher the gas concentration, the greater the number of opportunities for the water mist to absorb gas particles.
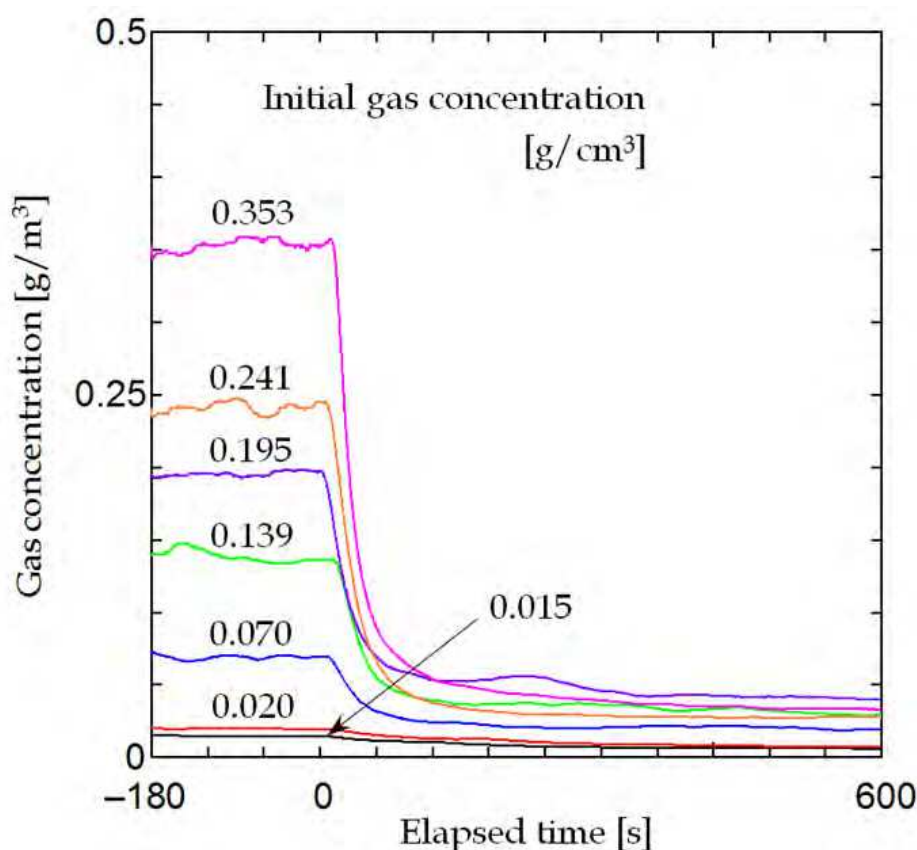

Fig. 21. Relationship between elapsed time and gas concentration. The input electric power is 50 W, the amount of water mist of large particles is 2.78 cm³/s, the amount of water mist of small particles is 0.27 cm³/s, and the driving frequency is 19.8 kHz.
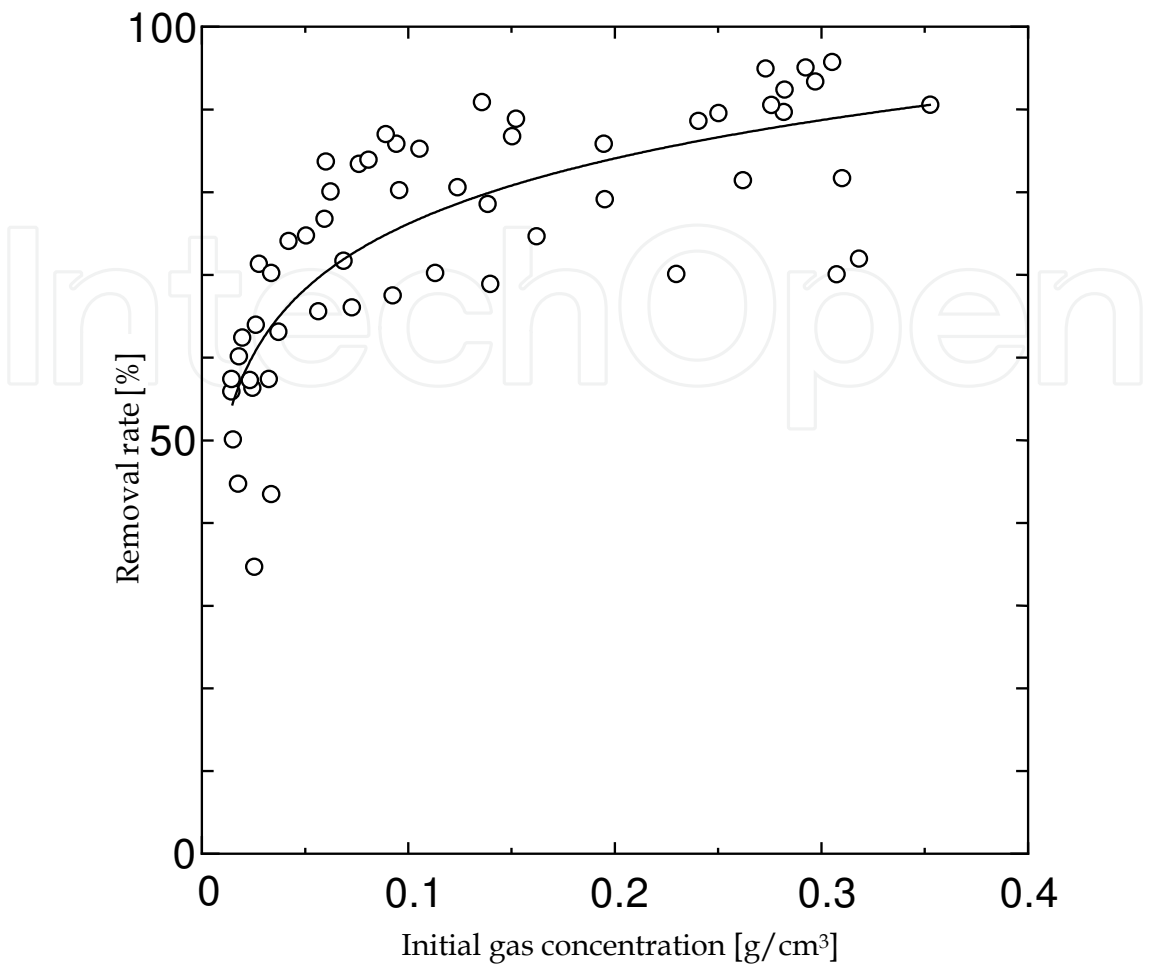
Fig. 22. Relationship between initial gas concentration and removal rate. The input electric power is 50 W, the amount of water mist of large particles is 2.78 cm³/s, the amount of water mist of small particles is 0.27 cm³/s, and driving frequency is 19.8 kHz.

3.4 Summary

In this section, I examined the effect on the increase in gas removal rate obtained when a low-hydrophilicity gas was absorbed and aggregated by irradiating aerial ultrasonic waves onto water mist of large particles (average particle diameter, approximately 60 μm) formed by the vibration of the plate and water mist of small particles (average particle diameter, approximately 3 μm) generated using a water spray system.

The following findings were obtained.

1. Even a low-hydrophilicity gas was effectively removed by the combined use of ultrasonic waves and water mist.
2. The gas removal rate increased when two kinds of water mist of large and small particles were simultaneously used.
3. When the amount of water mist of large particles was constant, the gas removal rate increased with the electric power input to the transducer and the amount of water mist of small particles for the ranges of input power and amount examined in this study.

4. When the amount of water mist of small particles was constant, the gas removal rate tended to increase with the electric power input to the transducer and the amount of water mist of large particles.
5. When the two kinds of water mist of large and small particles were used and subjected to ultrasonic irradiation, the gas removal rate increased with the initial gas concentration.
6. The gas removal rate reached approximately 90% when the amounts of water mist of small and large particles were 0.27 and 2.78 cm^3/s, respectively, and the electric power input to the transducer was 50 W.

From these results, it was found that a gas can be effectively removed by irradiating ultrasonic waves onto water mist of both large and small particles.

4. Conclusion

In this chapter, I described a method of designing square plates vibrating flexurally in the lattice mode that can be used as an intense aerial ultrasonic source, as well as the vibration mode of the fabricated plates. The distributions of the vibration displacement of the fabricated plates and the sound pressure near the plate surface were also described. In addition, the validity of the ultrasonic source was verified by theoretically and experimentally determining the directivity of the sound waves radiated from the vibrating plates into remote acoustic fields.

As an application of intense aerial ultrasonic waves, the enhancement of the removal of an unnecessary gas was examined. It was demonstrated that up to 90% of the gas was removed when aerial ultrasonic waves were irradiated onto water mist of large particles (average particle diameter, approximately 60 μm) formed by the flexural vibration of the plate and water mist of small particles (average particle diameter, approximately 3 μm) separately generated using a water spray system.

Thus, the use of aerial ultrasonic energy to remove unwanted gases appears to be promising; however, many unclear points still remain. Their clarification is expected to lead to an expansion in the range of applications of ultrasonic energy.

5. References

Asami, T. & Miura, H. (2010). Longitudinal Vibration Characteristics Required to Cut a Circle by Ultrasonic Vibration. *Japanese Journal of Applied Physics,* Vol. 49, 07HE23, (July 2010), pp. 07HE23-1-7

Asami, T. & Miura, H. (2011). Vibrator Development for Hole Machining by Ultrasonic Longitudinal and Torsional Vibration. *Japanese Journal of Applied Physics,* Vol. 50, 07HE31, (July 2010), pp. 07HE31-1-9

David, J. & Cheeke, N. (2002). *Fundamentals and applications of ultrasonic waves,* CRC Press, ISBN 0-8493-0130-0, Florida, USA.

Ito, Y. (2005). Experimental Investigation of Deflection of High-Speed Water Current with Aerial Ultrasonic Waves. *Japanese Journal of Applied Physics*, Vol. 44, Part 1, No. 6B, (June 2005), pp. 4669-4673.
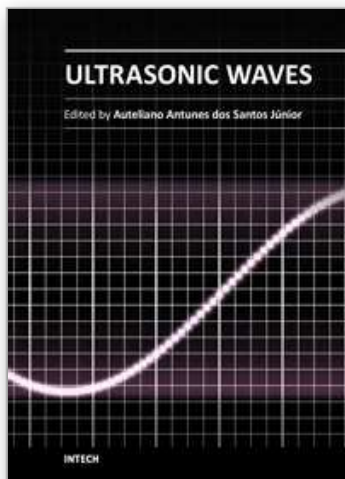
Ito, Y. & Takamura, E. (2010). Removal of Liquid in a Long Pore Opened at Both Ends Using High-Intensity Aerial Ultrasonic Waves. *Japanese Journal of Applied Physics*, Vol. 49, 07HE22, (July 2010), pp. 07HE22-1-6.

Kobayashi, M., Kamata, C. & Ito, K. (1997). Cold Model Experiments of Gas Removal from Molten Metal by an Irradiation of Ultrasonic Waves. *The Iron and Steel Institute of Japan (ISIJ) International,* Vol. 37, No. 1, (January 1997), pp. 9-1 5.

Lang, R. J. (1962). Ultrasonic Atomization of Liquids. *The Journal of the Acoustical Society of America*, Vol. 34, No. 1, (January 1962), pp. 6-8.

Miura, H. (1994). Aerial Ultrasonic Vibration Source using a Square Plate Vibrating in a Transverse Lattice-Mode. *The Journal of the Acoustical Society of Japan*, Vol. 50, No. 9, (September 1994), pp. 677-684.[in Japanese]

Miura, H., & Honda, Y. (2002). Aerial Ultrasonic Source Using a Striped Mode Transverse Vibrating Plate with Two Driving Frequencies. *Japanese Journal of Applied Physics,* Vol. 41, Part 1, No. 5B, (May 2002), pp. 3223-3227.

Miura, H. (2003). Eggshell Cutter Using Ultrasonic Vibration. *Japanese Journal of Applied Physics,* Vol. 42, Part 1, No.5B, (May 2003), pp. 2996-2999.

Miura, H. (2004). Promotion of Sedimentation of Dispersed Fine Particles Using Underwater Ultrasonic Wave. *Japanese Journal of Applied Physics,* Vol. 43, Part 1, No. 5B, (May 2004), pp. 2838-2839.

Miura, H., Takata, M., Tajima, D. & Tsuyuki, K. (2006). Promotion of Methane Hydrate Dissociation by Underwater Ultrasonic Wave. *Japanese Journal of Applied Physics,* Vol. 45, No. 5B, (May 2006), pp.4816-4823.

Miura, H. (2007a). Removal of Unnecessary Gas by Spraying Water Particles Formed by Aerial Ultrasonic Waves. *Japanese Journal of Applied Physics,* Vol. 46, No. 7B, (July 2007), pp. 4926-4930.

Miura, H. (2007b). Atomization of High-Viscosity Materials by One Point Convergence of Sound Waves Radiated from an Aerial Ultrasonic Source using a Transverse Vibrating Plate. *The 19th International Congress on Acoustics*, (September 2007), ULT-09-017.

Miura, H. (2008). Vibration Characteristics of Stepped Horn Joined Cutting Tip Employed in Circular Cutting Using Ultrasonic Vibration. *Japanese Journal of Applied Physics*, Vol. 47, No. 5, (May 2008), pp. 4282-4286.

Miura, H. & Ishikawa, H. (2009). Aerial Ultrasonic Source Using Stripes-Mode Transverse Vibrating Plate with Jutting Driving Point. *Japanese Journal of Applied Physics,* Vol. 48, 07GM10, (July 2009), pp. 07GM10-1-4.

Onishi, Y. & Miura, H. (2005). Convergence of Sound Waves Radiated from Aerial Ultrasonic Source Using Square Transverse Vibrating Plate with Several Reflective Boards. *Japanese Journal of Applied Physics,* Vol. 44, No. 6B, (June 2005), pp. 4682-4688.

Ueha, S., Maehara, N. & Mori,E. (1985). Mechanism of Ultrasonic Atomization using a Multipinhole Plate. *Journal of the Acoustical Society of Japan (E)*, Vol. 6, No. 1, (January 1985), pp. 21-26.

Yamane, H., Ito, Y., & Kawamura, M. (1983). Sound Radiation from Rectangular Plate Vibrating in Stripes Mode. *The Journal of the Acoustical Society of Japan*, Vol. 39, No. 6, (June 1983), pp. 380-387.[in Japanese]

Ultrasonic Waves

Edited by Dr Santos

Ultrasonic waves are well-known for their broad range of applications. They can be employed in various fields of knowledge such as medicine, engineering, physics, biology, materials etc. A characteristic presented in all applications is the simplicity of the instrumentation involved, even knowing that the methods are mostly very complex, sometimes requiring analytical and numerical developments. This book presents a number of state-of-the-art applications of ultrasonic waves, developed by the main researchers in their scientific fields from all around the world. Phased array modelling, ultrasonic thrusters, positioning systems, tomography, projection, gas hydrate bearing sediments and Doppler Velocimetry are some of the topics discussed, which, together with materials characterization, mining, corrosion, and gas removal by ultrasonic techniques, form an exciting set of updated knowledge. Theoretical advances on ultrasonic waves analysis are presented in every chapter, especially in those about modelling the generation and propagation of waves, and the influence of Goldberg's number on approximation for finite amplitude acoustic waves. Readers will find this book ta valuable source of information where authors describe their works in a clear way, basing them on relevant bibliographic references and actual challenges of their field of study.

How to reference

In order to correctly reference this scholarly work, feel free to copy and paste the following:

Hikaru Miura (2012). Intense Aerial Ultrasonic Source and Removal of Unnecessary Gas by the Source, Ultrasonic Waves, Dr Santos (Ed.), ISBN: 978-953-51-0201-4, InTech, Available from:
http://www.intechopen.com/books/ultrasonic-waves/intense-aerial-ultrasonic-source-and-removal-of-unnecessary-gas-by-the-source

INTECH
open science | open minds